X-ray Absorption Spectroscopy as a Probe of Ligand Noninnocence in Metallocorroles: The Case of Copper Corroles

Hyeongtaek Lim,[†] Kolle E. Thomas,[‡] Britt Hedman,*[,§] Keith O. Hodgson,*[,†,§] Abhik Ghosh,*[,‡] and Edward I. Solomon*[,†,§]

[†]Department of Chemistry, Stanford University, Stanford, California 94305;
[‡]Department of Chemistry, UiT – The Arctic University of Norway, N-9037 Tromsø, Norway;
[§]Stanford Synchrotron Radiation Lightsource, SLAC National Accelerator Laboratory, Stanford University, Menlo Park, California 94025.

ABSTRACT

An electronic structure and a Cu oxidation state of Cu corroles have been widely debated research topics due to the noninnocent ligand character of corroles. This study utilizes Cu K-edge X-ray absorption spectroscopy (XAS) to directly investigate the metal center of Cu corroles. The Cu K-edge XAS spectra of Cu corroles are compared to those of analogous Cu(II) porphyrins and time-dependent density functional theory calculations are performed to analyze the pre-edge regions. The results show that the Cu centers of Cu corroles are somewhat more oxidized relative to those of Cu(II) porphyrins but still retain significant Cu(II) characters.

INTRODUCTION

Although superficially similar, porphyrins and corroles exhibit major differences with respect to their coordination behavior. The differences reflect different formal charges, 3– for corroles versus 2– for porphyrins, and different N_4 cavity sizes for the two ligand families. As trianionic ligands with constricted N_4 cavities, corroles form a wide range of formally high-valent transition metal complexes.[1,2,3] The metal centers in many of these corrole complexes, however, are not truly high-valent; instead the corrole ligand is often partially oxidized, i.e., noninnocent. The phenomenon of ligand noninnocence is particularly common among first-row transition metal corroles[4,5,6,7,8,9] and Cu corroles provide some of the most intensively studied examples. A variety of experimental and computational approaches have been used to shed light on the noninnocent character of Cu corroles, which may be summarized as follows.

Simple, sterically unhindered Cu corroles are generally EPR-inactive at low temperature and exhibit diamagnetic ^{1}H NMR spectra at or below room temperature.[10,11] Above room temperature, however, their ^{1}H NMR spectra indicate the presence of a thermally accessible paramagnetic state, suggesting an $S = 1$ excited state.[12,13,14,15,16] Sterically hindered Cu corroles generally do not exhibit such temperature-dependent behavior, consistent with a higher singlet-triplet gap.

Hybrid densify functional theory (DFT) calculations on Cu corroles, sterically hindered or not, invariably yield a broken symmetry spin density profile, consistent with significant Cu(II)-corrole$^{\bullet 2-}$ character.[1,17,18]

The Soret maxima of Cu *meso*-tris(*para*-X-phenyl)corrole derivatives, Cu[T*p*XPC], exhibit pronounced redshifts with increasing electron-donating character of the *meso*-aryl *para* substituent X.[10,14,19] Over a long series of studies, this simple spectroscopic probe has emerged as a highly reliable signature of noninnocent metallocorroles.[3-10,20] In contrast, the Soret maxima of innocent metallotriarylcorroles, including MoO,[21] RuN,[22] OsN,[23] TcO,[24] ReO,[25] and Au[18,26,27,28] corroles as well as Mo[29] and W biscorroles,[30] are largely insensitive to the nature of the *para* substituent X.

Some of the most striking evidence for noninnocent corrole ligands comes from structural studies. Because of the rigidity of the direct C_1-C_{19} pyrrole-pyrrole linkage, metallocorroles are generally highly resistant to nonplanar distortions such as ruffling and saddling. Yet, even sterically unhindered Cu corroles are inherently saddled, as required for a Cu(d_{x2-y2})-corrole(π)

orbital interaction,[31] while sterically hindered, undecasubstituted Cu corroles are generally dramatically saddled.[18,32,33,34,35,36] In contrast, other metals (with the possible exception of Ag[18]) result in essentially planar macrocycle conformations, again emphasizing the key importance of Cu(d_{x2-y2})-corrole(π) orbital interaction.

Finally, electrochemical and spectroelectrochemical studies on coinage metal corroles strongly suggest a noninnocent formulation for Cu corroles and an innocent one for Au corroles.[18,37]

Despite the extensive body of evidence for a noninnocent corrole ligand in Cu corroles, one method that affords a direct probe of the metal center – X-ray absorption spectroscopy (XAS) – has not yet been applied to these complexes. Herein, we present such measurements on three Cu corroles, Cu[TPC], Cu[Br_8TPC], and Cu[$(CF_3)_8$TPC] (TPC = *meso*-triphenylcorrole), as well as on the bona fide Cu(II) porphyrins, Cu[TPP], Cu[Br_8TPP], and Cu[$(CF_3)_8$TPP] (TPP = *meso*-tetraphenylporphyrin) (Chart 1). Recently, XAS measurements on Mn,[38] Fe,[39] Co,[40] and Ag[41] corrole complexes have led to significant insights into the question of ligand noninnocence in these complexes. The present measurements, together with time-dependent density functional theory (TDDFT) analyses, have now shed considerable light on the electronic character of Cu corroles, underscoring yet again the considerable potential of XAS in elucidating the electronic structures of metalloporphyrin-type complexes.

Chart 1. Structures of Cu Corroles and Cu porphyrins Used in This Study

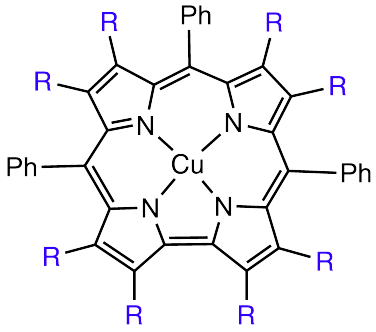

R = H: Cu[TPC]
R = Br: Cu[Br_8TPC]
R = CF_3: Cu[(CF_3)TPC]

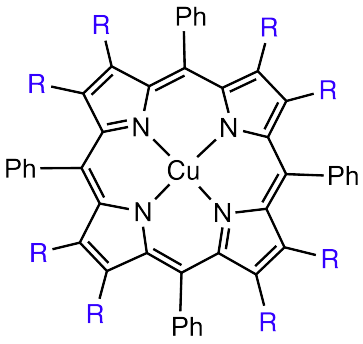

R = H: Cu[TPP]
R = Br: Cu[Br_8TPP]
R = CF_3: Cu[(CF_3)TPP]

RESULTS AND DISCUSSION

Cu K-edge X-ray absorption spectroscopy. In metal K-edge XAS, the rising-edge energy position has been used to investigate the oxidation state of the absorbing metal center.[42] Figure 1A shows the rising-edge regions of the three Cu corroles. These are shifted to somewhat higher energies relative to their Cu(II) porphyrin counterparts. Specifically, the features at ~8986 eV and ~8993 eV are assigned as a Cu 1s → 4p+ ligand-to-metal charge transfer shakedown transition and a Cu 1s → 4p transition, respectively.[43] These show upshifts of 0 – 1 eV in the Cu corroles relative to the Cu(II) porphyrins. This energy shift is rather small for a change in oxidation state from Cu(II) to Cu(III). By comparison, a previous study on Cu(II)/Cu(III) model complexes pairs revealed ~1 – 2 eV energy shifts in the rising-edge region.[44] The present results suggest that the metal centers in the Cu corroles are more oxidized than those in the Cu(II) porphyrins, but not to the level of authentic Cu(III) complexes. The energy shift in the rising-edge region, however, cannot be used as an authoritative analytic marker for distinguishing Cu(II) and Cu(III) complexes, since it varies significantly (by ~0 – 2 eV) among different pairs of complexes.[21]

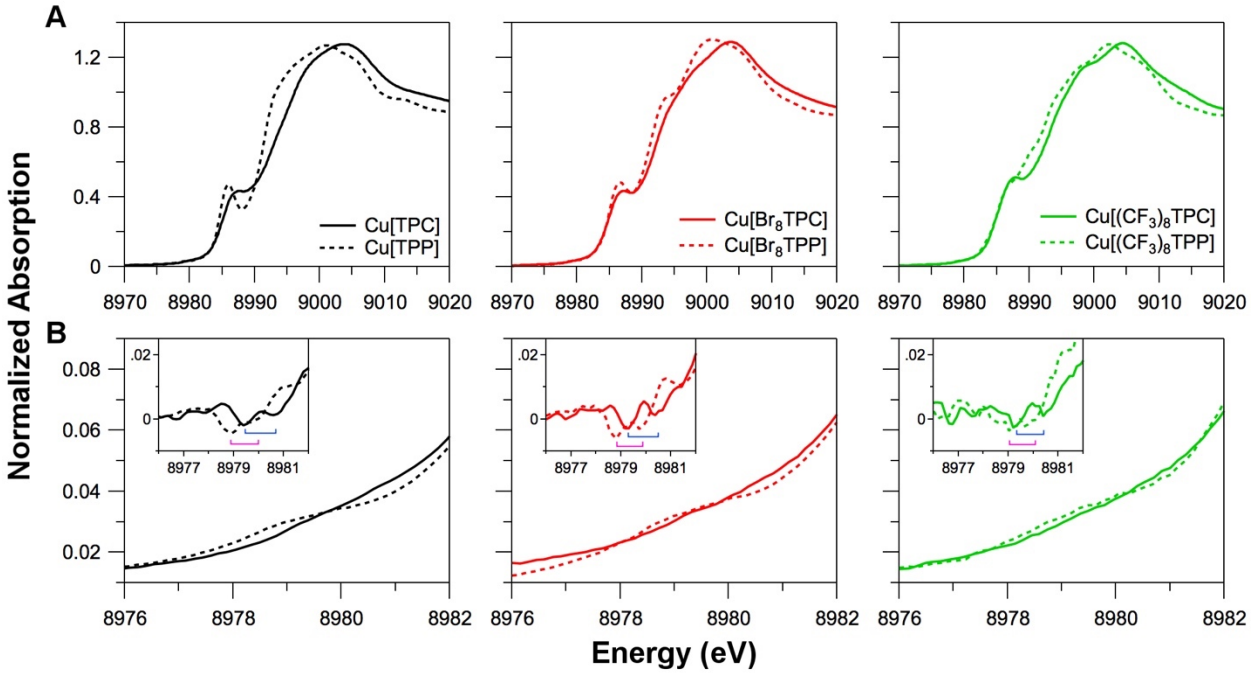

Figure 1. Cu K-edge XAS spectra (A) and the expanded pre-edge regions (B) of Cu[TPC] (solid black), Cu[TPP] (dotted black), Cu[Br_8TPC] (solid red), Cu[Br_8TPP] (dotted red), Cu[$(CF_3)_8$TPC]

(solid green), and Cu[$(CF_3)_8$TPP] (dotted green). Insets show the smoothed second derivative of the pre-edge region. Presence of two peaks in the pre-edge region is indicated in the insets (blue brackets for corroles and purple brackets for porphyrins).

In contrast, the Cu K pre-edge feature, which originates from a Cu 1s → 3d transition, provides a more direct measure of the Cu oxidation state. Typically, the pre-edge features of Cu(II) and Cu(III) complexes fall at ~8979 eV and ~8981 eV, respectively; thus, a ~2 eV shift is observed for an oxidation state change from Cu(II) to Cu(III) (see example in Figure S1).[21] Figure 1B presents the pre-edge features for both the Cu corroles and the Cu(II) porphyrins. Because the features are broad and weak, they have also been presented as their second derivatives (insets within Figures 1B). The insets within Figure 1B clearly show that there are two peaks in the pre-edge regions for both the Cu corroles and the Cu(II) porphyrins (indicated by horizontal brackets in the Figure 1B insets). These two peaks are split by 0.8 – 1.3 eV (Table 1). From the Cu(II) porphyrin to the corresponding Cu corrole, the energies of both peaks upshift, the first by 0.6 – 0.8 eV and the second by 0.8 – 1.1 eV (Table 1). A Cu K pre-edge region with two peaks is quite unusual and accordingly the assignment of the peaks is considered in the next section. The key point, however, is that the shifts in each of the porphyrin/corrole pairs are on the order of 0.6 – 1.1 eV, which is ~50% of those observed upon going from Cu(II) to Cu(III) in well-defined complexes. Thus, the Cu K-edge XAS spectra show that while the metal sites in the Cu corroles are more oxidized than those in their Cu(II) porphyrin analogs, they are not oxidized to the Cu(III) level.

Table 1. XAS Pre-edge Energies[a]

	peak 1 (eV)	peak 2 (eV)
Cu[TPC]	8979.7	8980.9
Cu[Br_8TPC]	8979.3	8980.6
Cu[$(CF_3)_8$TPC]	8979.3	8980.5
Cu[TPP]	8978.9	8979.9
Cu[Br_8TPP]	8978.7	8979.5
Cu[$(CF_3)_8$TPP]	8978.7	8979.7

[a]Pre-edge peaks were modeled using EDG_FIT as described in the experimental section. Peak energies are listed at maximum.

Time-dependent density functional theory analysis. TDDFT has been shown to provide reasonably good simulations of experimentally observed metal pre-edge regions and accordingly can be used for spectral assignment and quantitative analysis.[45, 46, 47,48] For assigning the two peaks observed in the pre-edge region, TDDFT calculations with the BP86 functional are first considered for the Cu(II) porphyrins (red spectra in Figure S2A, B, and C). It may be noted that the absorption energies in the TDDFT calculations are different from those in the experimental data. This is a well-known error in the DFT calculations which have limitations in modeling the potentials at the nucleus. The difference in the calculated and experimental absorption energies depends on the functional and the basis set used, but the error is systematic thus can be calibrated for the particular functional and basis set. In the present study, this issue is not of concern, since only energy differences among peaks are considered. In the TDDFT/BP86 calculations (red spectra in Figure S2A, B, and C), two transitions contribute to the peak at ~8952.3 eV for the Cu(II) porphyrins (Table 2; note that features at >8954 eV are part of the rising-edge region): one is the Cu 1s → $3d_{x2-y2}$ transition and the other is the Cu 1s → porphyrin $\pi^*(e_g)$ transitions. Figure 2A and Figure 3A, B, and C show the energy level diagram and the unoccupied molecular orbitals, respectively, associated with these valence levels. Although having two transitions in the pre-edge region in the TDDFT calculation is consistent with the two observed experimental peaks, their energy separation with the BP86 functional (0% Hartree-Fock (HF) exchange) is ~0.7 eV smaller than the experimental value (~1 eV) (Table 1 and Table 2). DeBeer and coworkers systematically compared the experimental and TDDFT calculated pre-edge regions for a series of Mn complexes and showed that the energy position of a Mn 1s → ligand π^* transition relative to that of a Mn 1s → 3d transition is highly dependent on the amount of HF exchange used in the TDDFT calculations.[24] Thus, TDDFT calculations with varying amounts of HF exchange were performed on the Cu(II) porphyrins to determine the amount of HF exchange required to simulate the experimental spectra (Figure 1 for the experimental spectra; Figure S2 and Figure 4 for the TDDFT simulations). TDDFT with the B3LYP functional (20% HF exchange) also shows two transitions: one at ~8987 eV (Cu 1s → $3d_{x2-y2}$) and the other at ~8991 – 8992 eV (Cu 1s → porphyrin π^*); these are separated by ~4 – 5 eV which is much larger than the experimentally observed energy splitting of ~1 eV (Table 2 and red spectra in Figure S2G, H,

and I). This energy separation becomes smaller as the amount of HF exchange decreases. Two transitions are calculated at ~8971 eV and ~8973 eV with 10% HF exchange (Table 2 and red spectra in Figure S2D, E, and F), showing an ~2 eV energy separation that is still larger than the experimental value. It is found that the experimental splittings of ~1 eV are reproduced with TDDFT calculations containing 5% HF exchange (Table 2 and red spectra in Figure 4).

Table 2. TDDFT Calculated Energies

% HF exchange	transitions	Cu[TPC]	Cu[Br_8TPC]	Cu[$(CF_3)_8$TPC]	Cu[TPP]	Cu[Br_8TPP]	Cu[$(CF_3)_8$TPP]
0%	1s → 3d	8952.9	8952.5	8952.4	8952.5	8952.2	8952.2
	1s → π^*[a]	8953.9	8953.3	8952.8	8952.9	8952.6	8952.1
5%	1s → 3d	8962.5	8962.1	8962.1	8961.8	8961.7	8961.7
	1s → π^*[a]	8964.2	8963.5	8963.0	8963.2	8962.9	8962.4
10%	1s → 3d	8971.7	8971.5	8971.5	8970.8	8970.8	8970.9
	1s → π^*[a]	8974.2	8973.5	8973.0	8973.3	8973.0	8972.5
20%	1s → 3d	8987.7	8987.5	8987.5	8986.9	8987.0	8987.2
	1s → π^*[a]	8992.2	8991.8	8991.3	8991.7	8991.4	8990.9
	1s → cor b_1[b]	8989.6	8989.8	8989.9	-	-	-

[a]This is the Cu 1s → corrole/porphyrin π^* transition and its listed energy is an intensity-weighted average energy position. [b]Corrole is denoted by cor.

The Cu corroles also exhibit two pre-edge peaks split by 1.2 – 1.3 eV (as shown by the experimental spectra in solid lines in Figure 1) and TDDFT calculations with 0 – 20% HF exchange were again performed to assign these peaks (Table 2 and black spectra in Figure S2 and Figure 4). As for the Cu(II) porphyrins, TDDFT calculations with 5% HF exchange satisfactorily reproduce the experimental spectra (Table 2 and black spectra in Figure 4), yielding a splitting of ~1.3 eV between the two transitions. The assignment of these two peaks is very similar to that for the Cu(II) porphyrins: one is the Cu 1s → $3d_{x2-y2}$ transition and the other corresponds to near-degenerate Cu 1s → corrole π^* (a_2 + b_1) transitions; these valence levels are shown in Figure 2B and C, and the relevant molecular orbitals are shown in Figure 3D, E, and F. As in the case of the Cu(II) porphyrins, the energy separation between these two transitions increases with increasing amounts of HF exchange. It is important to note that in TDDFT with

20% HF exchange for the Cu corroles but not for the Cu(II) porphyrins there is an additional feature at ~8989.8 eV which appears ~2 eV higher than the Cu 1s → $3d_{x2-y2}$ transition (indicated by arrows in Figure S2G, H, and I). In the TDDFT calculations with 20% HF exchange, there is spin polarization of the energy level diagram due to the increased exchange (Figure 2C). Specifically, the electrons in the b_1-HOMO of the Cu corroles are spin-polarized and this leads to a hole in the corrole b_1 orbital (note that the corrole b_1-HOMO is analogous to the porphyrin a_{2u}-HOMO) and an electron in the Cu $3d_{x2-y2}$ orbital. Thus, the additional feature at ~8989.8 eV originates from a new possible transition from the Cu 1s orbital to the corrole b_1 orbital. Alternatively, the TDDFT calculations with 0 – 10% HF exchange do not exhibit this additional feature (Table 2 and black spectra in Figure S2A – F and Figure 4), since the amount of the exact exchange is not high enough to result in significant spin polarization; two electrons thus occupy the corrole b_1-HOMO while the Cu $3d_{x2-y2}$ orbital is empty (Figure 2B).

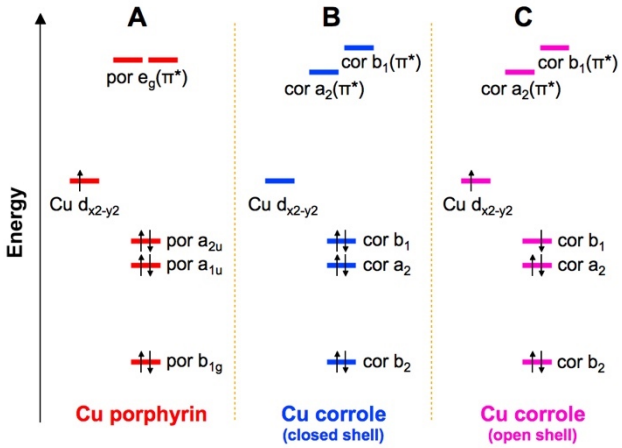

Figure 2. Schematic energy level diagram for Cu porphyrin (A) and Cu corrole (B and C) (por and cor denote porphyrin and corrole, respectively). For Cu corrole, two possible electronic structures are shown: (B) closed-shell description (two electrons are in corrole b_1 with empty Cu d_{x2-y2}) and (C) open-shell description (one electron transferred from corrole b_1 to Cu d_{x2-y2} giving antiferromagnetic exchange coupling).

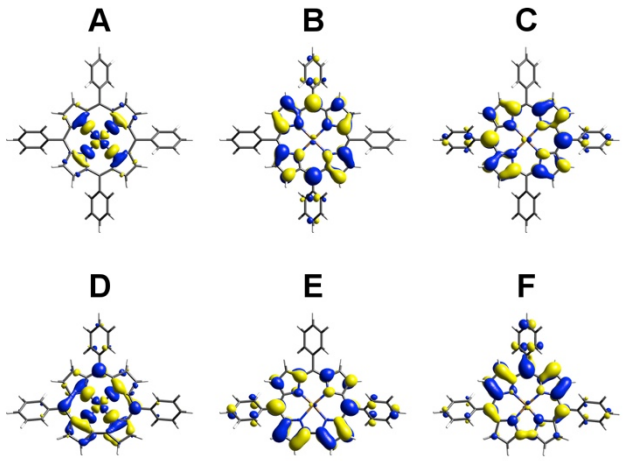

Figure 3. Contour plots of unoccupied molecular orbitals which are associated with two peaks in the pre-edge regions for Cu[TPP] (A, B, and C) and Cu[TPC] (D, E, and F). A and D are molecular orbitals having significant Cu $3d_{x2-y2}$ characters for Cu[TPP] and Cu[TPC], respectively. B, C, E, and F are porphyrin/corrole π^* orbitals (B and C for e_g of Cu[TPP]; E and F for a_2 and b_1, respectively, of Cu[TPC]).

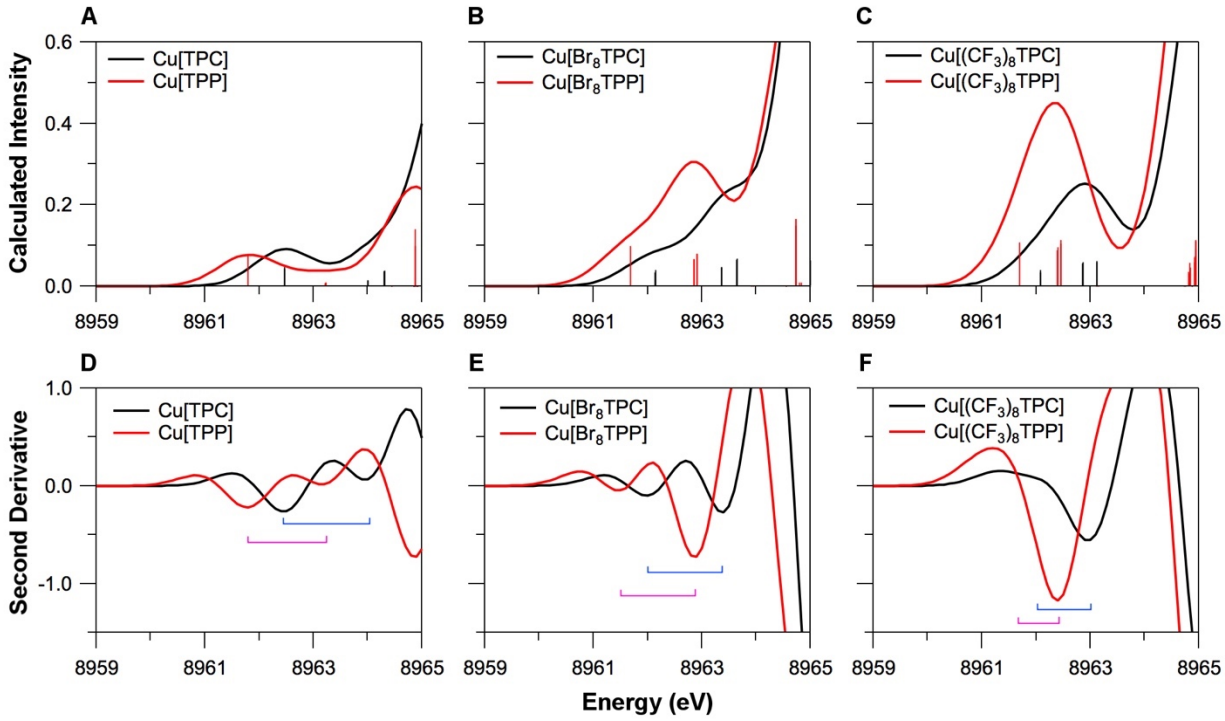

Figure 4. Pre-edge regions (A, B, and C) and their second derivatives (D, E, and F) calculated using TDDFT with 5% HF exchange. Presence of two peaks in the pre-edge region is indicated in the second derivative plots by blue brackets for corroles and purple brackets for porphyrins.

CONCLUDING REMARKS

The issues of ligand noninnocence in Cu coroles has been addressed in many studies. In this study, Cu K-edge XAS has been used to probe the Cu oxidation state in the Cu corroles and the analogous Cu(II) porphyrins. The XAS data revealed two peaks in the pre-edge regions for both classes of complexes; the lower- and higher-energy peaks were assigned to the Cu 1s → $3d_{x2-y2}$ and Cu 1s → corrole/porphyrin π^* transitions, respectively, by means of TDDFT calculations (Figure 2). The oxidation state of the Cu center can be directly related to the energy position of the lower-energy peak. For the Cu(II) porphyrins, the Cu 1s → $3d_{x2-y2}$ transition occurs at 8978.9 eV, 8978.7 eV, and 8978.7 eV for Cu[TPP], Cu[Br_8TPP], and Cu[$(CF_3)_8$TPP], respectively (Figure 1 and Table 1). For the corresponding Cu corroles, the Cu 1s → $3d_{x2-y2}$ transitions are upshifted to 8979.7 eV, 8979.3 eV, and 8979.3 eV, respectively. In other words, the porphyrin-to-corrole upshifts are 0.8 eV, 0.6 eV, and 0.6 eV for the β-H_8, β-Br_8, and β-$(CF_3)_8$ substitution patterns, respectively. These energy upshifts are all less than half that for a genuine oxidation state change from Cu(II) to Cu(III) (~2 eV). The Cu centers of the Cu corroles thus are best described as somewhat oxidized relative to the Cu(II) porphyrin, but not up to a Cu(III) state.

Two mechanisms can account for a Cu(II)-like center in Cu corroles: (1) strong covalent interaction between the Cu $3d_{x2-y2}$ orbital and the corrole N lone-pair based molecular orbital whose energy level is schematically shown as b_2 in Figure 2 (analogous to porphyrin b_{1g}), and (2) electron donation from the corrole b_1-HOMO (analogous to the porphyrin a_{2u}-HOMO) into the Cu $3d_{x2-y2}$ orbital. It has been suggested that the substantial saddling of Cu corroles, which facilitates the otherwise symmetry-forbidden Cu($3d_{x2-y2}$)-corrole(b_1-HOMO) orbital interaction (a σ-π interaction) (Figure 5), would lead to a spin polarization (one electron in the Cu $3d_{x2-y2}$ orbital and the other in the corrole b_1 orbital) which reflects antiferromagnetic coupling.[6,11-15] In this regard, the second mechanism has been proposed to be dominantly responsible for the Cu(II) character in Cu corroles. This has been supported by other experimental and calculational data including the strong substituent dependence of the Soret maxima,[10] the temperature dependence of ^{1}H NMR indicating the presence of a thermally accessible triplet state,[4] and the relatively high

reduction potentials.[8] The present study shows that the experimental Cu K pre-edge features are best reproduced with TDDFT calculations with 5% HF exchange which does not give spin polarization. This may suggest that the first mechanism also significantly contributes to the Cu(II) character of Cu corroles. However, defining the relative importance between two mechanisms is beyond the scope of this study.

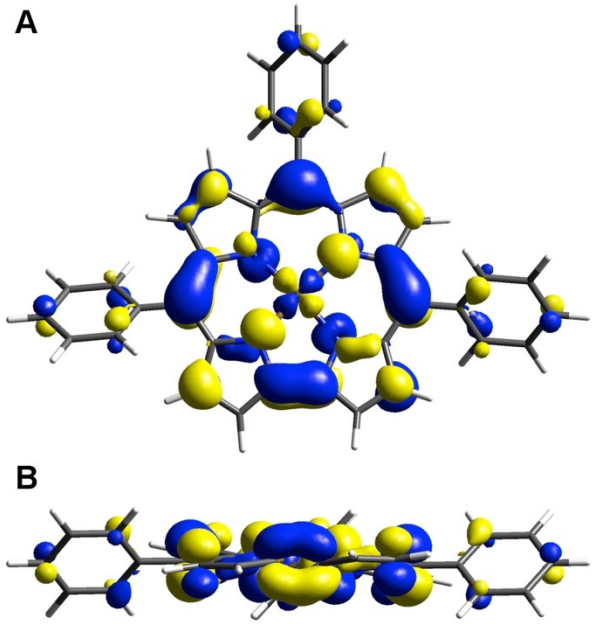

Figure 5. Contour plot of HOMO of Cu[TPC] from TDDFT with 5% HF exchange (A: top view and B: side view). This shows a σ-π interaction between the Cu $3d_{x2-y2}$ orbital and the corrole b_1-HOMO from saddling.

EXPERIMENTAL SECTION

Sample preparation. H_2TPP,[49] Cu[TPP],[50] Cu[Br_8TPP],[51] Cu[$(CF_3)_8$TPP],[52] H_3TPC,[53] Cu[TPC],[10] Cu[Br_8TPC],[10] and Cu[$(CF_3)_8$TPC][5,29] were prepared as previously described. The structures of these complexes were confirmed with UV-vis spectrophotometry, high resolution electrospray ionization mass spectrometry, and ^1H and ^{19}F NMR spectroscopy.

X-ray absorption spectroscopy. The Cu K-edge X-ray absorption spectra were collected at the Stanford Synchrotron Radiation Lightsource on the unfocused 20-pole 2 T wiggler beam line 7-3 under standard ring conditions of 3 GeV and ~500 mA. A Rh-coated premonochromator mirror was used for harmonic rejection and vertical collimation. A Si(220) double-crystal

monochromator was used for energy selection. Each solid sample was finely ground with BN and this homogeneous mixture was pressed into an Al spacer with 38 μm Kapton tape windows. The samples were maintained at a constant temperature of ~10 K during data collection using an Oxford Instruments CF 1208 continuous flow liquid helium cryostat. The transmission mode was used to collect data to $k = 9.5$ Å^{-1}. Internal energy calibration was accomplished by simultaneous measurement of the absorption of a Cu foil placed between ionization chambers situated after the sample. The inflection point of the foil spectrum was assigned to 8980.3 eV. Spectra presented here are 2 – 4 scan averaged data. To prevent any photodegradation effect in the final data, only the first scans obtained from physically separated measurement spots were used for the final average.

Background subtraction and normalization of the data were performed using PySpline.[54] The data were processed by fitting a second-order polynomial to the pre-edge region and subtracting this from the entire spectrum as a background. A two-region polynomial spline of orders 2 and 3 was used to model the smoothly decaying post-edge region. The data were normalized by scaling the spline function to an edge jump of 1.0 at 9000 eV.

The Cu K pre-edge features were modeled with pseudo-Voigt line shape with a 1:1 ratio of Lorentzian:Gaussian functions using the fitting program EDG_FIT (George, G. N. Stanford Synchrotron Radiation Laboratory: Stanford, CA, 2000). To reduce the number of the variables which float during the fitting process, the half width at half maximum (HWHM) for the Cu 1s → $3d_{x2-y2}$ transition peak was obtained using the Cu(II) model complexes, $[Cu(II)(H_{-2}Aib_3)]_2$ (Aib = tri-α-aminoisobutyric acid) and $[Cu(II)_2(\mu\text{-}OH)_2(L_{Me3\text{-}TACN})_2]^{2+}$ ($L_{Me3\text{-}TACN}$ = 1,4,7-trimethyl-1,4,7-triazacyclononane).[21] While this obtained HWHM value (0.91 eV) was kept constant for the low-energy peak in the experimental spectra, other variables including the HWHM of the high-energy peak, energy position, and peak intensity were all allowed to float throughout the fitting process. A function modeling the background was empirically chosen to give the best fit. An acceptable fit reasonably matches both the pre-edge spectrum and its second derivative. In all cases, three acceptable fits with different HWHM (±0.3 fixed from float) backgrounds were acquired over the energy ranges of 8976-8983, 8976-8984, and 8976-8985 eV resulting in a total of nine pre-edge fits per data set, which were averaged to get mean values.

Computational methods. The geometry optimizations were conducted with the ADF

program [55] using the BP86[56,57] functional. Grimme D3 dispersion correction was employed to account for the noncovalent interaction.[58] The TDDFT calculations for the pre-edge region analysis were performed with the ORCA 3.0.3 program[59] using the geometry optimized structures. The TDDFT calculations were conducted with the BP86 and B3LYP[60,61] functionals and the def2-TZVP[62] basis set. For the calculations with the 5% and 10% HF exchange, the amount of the HF exchange in the B3LYP functional was modified to 5% or 10%. The RIJCOSX approximation was used for the calculations with the hybrid functionals.[63] The zeroth-order regular approximation (ZORA)[64,65] for relativistic effects and the conductor like screening model (COSMO)[66] in an infinite dielectric were included. The calculations used a dense integration grid (ORCA Grid4) and tight convergence criteria. The TDDFT calculated transitions were broadened by a Gaussian function with 1.4 eV line width for comparison with the experimental spectra. Molecular orbitals were visualized with LUMO (Kieber-Emmons, M. T.: Ephrata, PA, 2012).

ASSOCIATED CONTENT

Supporting Information.

The Supporting Information is available free of charge.

Cu K-edge XAS spectra of $[Cu(II)(H_{-2}Aib_3)]_2$ and $Cu(III)(H_{-3}Aib_3)$, TDDFT calculated pre-edge regions with different amount of HF exchange (0%, 10%, and 20%), and DFT optimized Cartesian coordinates (PDF).

AUTHOR INFORMATION

Corresponding Author

*Email: hedman@slac.stanford.edu (B.H.)

*Email: hodgsonk@stanford.edu (K.O.H.)

*Email: abhik.ghosh@uit.no (A.G.)

*Email: edward.solomon@stanford.edu (E.I.S.)

Notes

The authors declare no competing financial interest.

ACKNOWLEDGMENT

H.L. was supported by an Abbott Laboratories Stanford Graduate Fellowship. For A.G., this work was supported by grants 231086 and 262229 of the Research Council of Norway. For E.I.S., research reported in this publication was supported by the National Institute of Diabetes and Digestive and Kidney Diseases of the National Institutes of Health under award number R01DK031450. Use of the Stanford Synchrotron Radiation Lightsource, SLAC National Accelerator Laboratory, is supported by the U.S. Department of Energy, Office of Science, Office of Basic Sciences under Contract No. DE-AC02-76SF00515. The SSRL Structural Molecular Biology Program is supported by the DOE Office of Biological and Environmental Research, and by the National Institutes of Health, National Institute of General Medical Sciences (including P41GM103393). The contents of this publication are solely the responsibility of the authors and do not necessarily represent the official views of NIGMS or NIH.

TABLE OF CONTENTS SYNOPSIS

Cu K-edge X-ray absorption spectroscopy, together with time-dependent density functional theory calculations, reveal that the metal center of Cu corroles has significant Cu(II) characters although corroles are trianionic ligands.

TABLE OF CONTENTS GRAPHIC

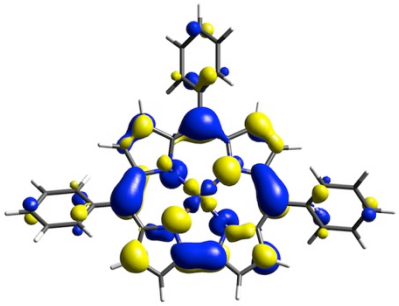

References

1.Thomas, K. E.; Alemayehu, A. B.; Conradie, J.; Beavers, C. M.; Ghosh, A. The Structural Chemistry of Metallocorroles: Combined X-ray Crystallography and Quantum Chemistry Studies Afford Unique Insights. *Acc. Chem. Res.* **2012**, *45*, 1203–1214.

2. Palmer, J. H. Transition Metal Corrole Coordination Chemistry. In *Molecular Electronic Structures of Transition Metal Complexes I*; Mingos, D. M. P., Day, P., Dahl, J. P., Eds.; Structure and Bonding; Springer Berlin Heidelberg: Berlin, Heidelberg, 2011; Vol. 142, pp 49–89.

3. Ghosh, A. Electronic Structure of Corrole Derivatives: Insights from Molecular Structures, Spectroscopy, Electrochemistry, and Quantum Chemical Calculations. *Chem. Rev.* **2017**, *117*, 3798–3881.

([4]) Steene, E.; Wondimagegn, T.; Ghosh, A. Electrochemical and Electronic Absorption Spectroscopic Studies of Substituent Effects in Iron(IV) and Manganese(IV) Corroles. Do the Compounds Feature High-Valent Metal Centers or Noninnocent Corrole Ligands? Implications for Peroxidase Compound I and II Intermediates. *J. Phys. Chem. B* **2001,** *105*, 11406-11413.

([5]) Ganguly, S.; McCormick, L. J.; Conradie, J.; Gagnon, K. J.; Sarangi, R.; Ghosh, A. Electronic Structure of Manganese Corroles Revisited: X-ray structures, Optical and X-ray Absorption Spectroscopies, and Electrochemistry as Probes of Ligand Noninnocence. *Inorg. Chem.* Article ASAP. DOI: 10.1021/acs.inorgchem.8b00537.

([6]) Ganguly, S.; Thomas, K. E.; Sarangi, R.; Ghosh, A. Ligand Noninnocence in Iron Corroles: Insights from Optical and X-ray Absorption Spectroscopies and Electrochemical Redox Potentials. *Chem. Eur. J*. **2017**, *23*, 15098-15106.

([7]) Vazquez-Lima, H.; Norheim, H. K.; Einrem, R. F.; Ghosh, A. Cryptic Noninnocence: FeNO Corroles in a New Light. *Dalton Trans*. **2015**, *44*, 10146-10151.

([8]) Norheim, H.-K.; Capar, J.; Einrem, R. F.; Gagnon, K. J.; Beavers, C. M.; Vazquez-Lima, H.; Ghosh, A. Ligand Noninnocence in FeNO Corroles: Insights from *β*-Octabromocorrole Complexes. *Dalton Trans.* **2016,** *45*, 681-689.

([9]) Ganguly, S.; Vazquez-Lima, H.; Ghosh, A. Wolves in Sheep's Clothing: *μ*-Oxo-Diiron Corroles Revisited. *Chem. Eur. J*. **2016**, *22*, 10336−10340.

10. Wasbotten, I. H.; Wondimagegn, T.; Ghosh, A. Electronic Absorption, Resonance Raman, and Electrochemical Studies of Planar and Saddled Copper(III) *meso*-Triarylcorroles. Highly

Substituent-Sensitive Soret Bands as a Distinctive Feature of High-Valent Transition Metal Corroles. *J. Am. Chem. Soc.* **2002**, *124*, 8104–8116.

11. Lemon, C. M.; Huynh, M.; Maher, A. G.; Anderson, B. L.; Bloch, E. D.; Powers, D. C.; Nocera, D. G. Electronic Structure of Copper Corroles. *Angew. Chem. Int. Ed.* **2016**, *55*, 2176–2180.

(12) Will, S.; Lex, J.; Vogel, E.; Schmickler, H.; Gisselbrecht, J. P.; Haubtmann, C.; Bernard, M.; Gross, M. Nickel and Copper Corroles: Well-Known Complexes in a New Light. *Angew. Chem., Int. Ed.* **1997**, *36*, 357–361.

(13) Brückner, C.; Briñas, R. P.; Bauer, J. A. K. X-ray Structure and Variable Temperature NMR Spectra of [*meso*-Triarylcorrolato]copper(III). *Inorg. Chem.* **2003**, *42*, 4495–4497.

([14]) Steene, E.; Dey, A.; Ghosh, A. *β*-Octafluorocorroles. *J. Am. Chem. Soc.* **2003,** *125*, 16300-16309.

(15) Luobeznova, I.; Simkhovich, L.; Goldberg, I.; Gross, Z. Electronic Structures and Reactivities of Corrole−Copper Complexes. *Eur. J. Inorg. Chem* **2004**, *2004*, 1724–1732.

16. Bröring, M.; Brégier, F.; Tejero, E. C.; Hell, C.; Holthausen, M. C. Revisiting the Electronic Ground State of Copper Corroles. *Angew. Chem., Int. Ed.* **2007**, *46*, 445–448.

(17) Pierloot, K.; Zhao, H.; Vancoillie, S. Copper Corroles: the Question of Noninnocence. *Inorg. Chem.* **2010**, *49*, 10316–10329.

(18) Thomas, K. E.; Vazquez-Lima, H.; Fang, Y.; Song, Y.; Gagnon, K. J.; Beavers, C. M.; Kadish, K. M.; Ghosh, A. Ligand Noninnocence in Coinage Metal Corroles: a Silver Knife-Edge. *Chem. - Eur. J.* **2015**, *21*, 16839–16847.

19. Thomas, K. E.; Wasbotten, I. H.; Ghosh, A. Copper *β*-Octakis(trifluoromethyl)corroles: New Paradigms for Ligand Substituent Effects in Transition Metal Complexes. *Inorg. Chem.* **2008**, *47*, 10469–10478.

([20]) Alemayehu, A. B.; Vazquez-Lima, H.; Beavers, C. M.; Gagnon, K. J.; Bendix, J.; Ghosh, A. Platinum Corroles. *Chem. Comm*. **2014**, *50*, 11093-11096.

([21]) Johansen, I.; Norheim, H.-K.; Larsen, S.; Alemayehu, A. B.; Conradie, J.; Ghosh, A. Substituent Effects on Metallocorrole Spectra: Insights from Chromium-Oxo and Molybdenum-Oxo Triarylcorroles. *J. Porphyrins Phthalocyanines* **2011**, *15*, 1335-1344.

([22]) Alemayehu, A. B.; Vazquez-Lima, H. Gagnon, K. J.; Ghosh, A. Stepwise Deoxygenation of Nitrite as a Route to Two Families of Ruthenium Corroles: Group 8 Periodic Trends and Relativistic Effects. *Inorg. Chem.* **2017***, 56*, 5285–5294.

([23]) Alemayehu, A. B.; Gagnon, K. J.; Terner, J.; Ghosh, A. Oxidative Metalation as a Route to Size-Mismatched Macrocyclic Complexes: Osmium Corroles. *Angew. Chem. Int. Ed*. **2014**, *53*, 14411-14414.

([24]) Alemayehu, A. B.; Vazquez-Lima, H. Gagnon, K. J.; Ghosh, A. Stepwise Deoxygenation of Nitrite as a Route to Two Families of Ruthenium Corroles: Group 8 Periodic Trends and Relativistic Effects. *Inorg. Chem.* **2017***, 56*, 5285–5294.

([25]) Einrem, R. F.; Gagnon, K. J.; Alemayehu, A. B.; Ghosh, A. Metal-Ligand Misfits: Facile Access to Rhenium-Oxo Corroles by Oxidative Metalation. *Chem. Eur. J.* **2016,** *22*, 517-520.

([26]) Alemayehu, A B.; Ghosh, A. Gold Corroles. *J. Porphyrins Phthalocyanines* **2011**, *15*, 106-110.

([27]) Rabinovitch, E.; Goldberg, I.; Gross, Z. Gold(I) and Gold(III) Corroles. *Chem. Eur. J*. **2011**, *17*, 12294–12301.

([28]) Thomas, K. E.; Alemayehu, A. B.; Conradie, J.; Beavers, C.; Ghosh, A. Synthesis and Molecular Structure of Gold Triarylcorroles. *Inorg. Chem.* **2011**, *50*, 12844–12851.

([29]) Alemayehu, A.; Vazquez-Lima, H.; McCormick, L. J.; Ghosh, A. Relativistic effects in metallocorroles: comparison of molybdenum and tungsten biscorroles. *Chem. Commun*. **2017**, *53*, 5830-5833

([30]) Alemayehu, A.; Vazquez-Lima, H.; Gagnon, K. J.; Ghosh, A. Tungsten Biscorroles: New Chiral Sandwich Compounds. *Chem. Eur. J.* **2016**, *22*, 6914-6920.

(31) Alemayehu, A. B.; Gonzalez, E.; Hansen, L. K.; Ghosh, A. Copper Corroles Are Inherently Saddled. *Inorg. Chem.* **2009**, *48*, 7794–7799.

32. Alemayehu, A. B.; Hansen, L. K.; Ghosh, A. Nonplanar, Noninnocent, and Chiral: a Strongly Saddled Metallocorrole. *Inorg. Chem.* **2010**, *49*, 7608–7610.

33. Thomas, K. E.; Conradie, J.; Hansen, L. K.; Ghosh, A. A Metallocorrole with Orthogonal Pyrrole Rings. *Eur. J. Inorg. Chem* **2011**, *2011*, 1865–1870.

[34] Berg, S.; Thomas, K. E.; Beavers, C. M.; Ghosh, A. Undecaphenylcorroles. *Inorg. Chem.* **2012,** *51*, 9911-9916.

[35] Thomas, K. E.; McCormick, L. J.; Carrié, D.; Vazquez-Lima, H.; Simmoneaux, G.; Ghosh, A. Halterman Corroles and Their Use as a Probe of the Conformational Dynamics of the Inherently Chiral Copper Corrole Chromophore. *Inorg. Chem*., Article ASAP. DOI: 10.1021/acs.inorgchem.7b02767.

[36] Thomassen, I. K.; M^{c}Cormick, L. J.; Ghosh, A. Synthesis and Molecular Structure of a Copper Octaiodocorrole. *ACS Omega*, **2018**, *3*, 5106–5110.

[37]. Ou, Z.; Shao, J.; Zhao, H.; Ohkubo, K.; Wasbotten, I. H.; Fukuzumi, S.; Ghosh, A.; Kadish, K. M. Spectroelectrochemical and ESR Studies of Highly Substituted Copper Corroles. *J. Porphyrins Phthalocyanines* **2004,** *8*, 1236-1247.

38. Ganguly, S.; McCormick, L. J.; Conradie, J.; Gagnon, K. J.; Sarangi, R.; Ghosh, A. Electronic Structure of Manganese Corroles Revisited: X-ray Structures, Optical and X-ray Absorption Spectroscopies, and Electrochemistry as Probes of Ligand Noninnocence. *Inorg. Chem*. **2018**, *57*, 9656-9669.

39. Ganguly, S.; Giles, L. J.; Thomas, K. E.; Sarangi, R.; Ghosh, A. Ligand Noninnocence in Iron Corroles: Insights from Optical and X-ray Absorption Spectroscopies and Electrochemical Redox Potentials. *Chem. - Eur. J.* **2017**, *23*, 15098–15106.

40. Ganguly, S.; Renz, D.; Giles, L. J.; Gagnon, K. J.; McCormick, L. J.; Conradie, J.; Sarangi, R.; Ghosh, A. Cobalt- and Rhodium-Corrole-Triphenylphosphine Complexes Revisited: the Question of a Noninnocent Corrole. *Inorg. Chem.* **2017**, *56*, 14788–14800.

41. Sarangi, R.; Giles, L. J.; Thomas, K. E.; Ghosh, A. Ligand Noninnocence in Silver Corroles: a XANES Investigation. *Eur. J. Inorg. Chem* **2016**, *2016*, 3225–3227.

42. Sarangi, R. X-ray Absorption Near-Edge Spectroscopy in Bioinorganic Chemistry: Application to M-O_2 Systems. *Coord. Chem. Rev.* **2013**, *257*, 459–472.

43. Kau, L. S.; Spira-Solomon, D. J.; Penner-Hahn, J. E.; Hodgson, K. O.; Solomon, E. I. X-ray Absorption Edge Determination of the Oxidation State and Coordination Number of Copper: Application to the Type 3 Site in *Rhus Vernicifera* Laccase and Its Reaction with Oxygen. *J. Am. Chem. Soc.* **1987**, *109*, 6433–6442.

44. DuBois, J. L.; Mukherjee, P.; Stack, T. D. P.; Hedman, B.; Solomon, E. I.; Hodgson, K. O. A Systematic K-edge X-ray Absorption Spectroscopic Study of Cu(III) Sites. *J. Am. Chem. Soc.* **2000**, *122*, 5775–5787.

45. George, S. D.; Petrenko, T.; Neese, F. Prediction of Iron K-edge Absorption Spectra Using Time-Dependent Density Functional Theory. *J. Phys. Chem. A* **2008**, *112*, 12936–12943.
46. Chandrasekaran, P.; Stieber, S. C. E.; Collins, T. J.; Lawrence Que, J.; Neese, F.; DeBeer, S. Prediction of High-Valent Iron K-edge Absorption Spectra by Time-Dependent Density Functional Theory. *Dalton Trans.* **2011**, *40*, 11070–11079.
47. Roemelt, M.; Beckwith, M. A.; Duboc, C.; Collomb, M.-N.; Neese, F.; DeBeer, S. Manganese K-edge X-ray Absorption Spectroscopy as a Probe of the Metal–Ligand Interactions in Coordination Compounds. *Inorg. Chem.* **2011**, *51*, 680–687.
48. Lima, F. A.; Bjornsson, R.; Weyhermüller, T.; Chandrasekaran, P.; Glatzel, P.; Neese, F.; DeBeer, S. High-Resolution Molybdenum K-edge X-ray Absorption Spectroscopy Analyzed with Time-Dependent Density Functional Theory. *Phys. Chem. Chem. Phys.* **2013**, *15*, 20911–20920.
49. Adler, A. D.; Longo, F. R.; Finarelli, J. D.; Goldmacher, J.; Assour, J.; Korsakoff, L. A Simplified Synthesis for *meso*-Tetraphenylporphine. *J. Org. Chem.* **1967**, *32*, 476–476.
50. Adler, A. D.; Longo, F. R.; Varadi, V. *Metalloporphyrins*; Basolo, F., Ed.; Inorganic Syntheses, 2006; Vol. 16, pp 213–220.
51. Bhyrappa, P.; Krishnan, V. Octabromotetraphenylporphyrin and Its Metal Derivatives: Electronic Structure and Electrochemical Properties. *Inorg. Chem.* **1991**, *30*, 239–245.
52. Liu, C.; Chen, Q. Y. Fluoroalkylation of Porphyrins: a Facile Synthesis of Trifluoromethylated Porphyrins by a Palladium-Catalyzed Cross-Coupling Reaction. *Eur. J. Org. Chem.* **2005**, *2005*, 3680–3686.
53. Koszarna, B.; Gryko, D. T. Efficient Synthesis of *meso*-Substituted Corroles in a H_2O−MeOH Mixture. *J. Org. Chem.* **2006**, *71*, 3707–3717.
54. Tenderholt, A.; Hedman, B.; Hodgson, K. O. PySpline: a Modern, Cross-Platform Program for the Processing of Raw Averaged XAS Edge and EXAFS Data. *AIP Conf. Proc.* **2007**, *882*, 105–107.
55. te Velde, G.; Bickelhaupt, F. M.; Baerends, E. J.; Fonseca Guerra, C.; van Gisbergen, S. J. A.; Snijders, J. G.; Ziegler, T. Chemistry with ADF. *J. Comput. Chem.* **2001**, *22*, 931–967.
56. Perdew, J. P. Density-Functional Approximation for the Correlation Energy of the Inhomogeneous Electron Gas. *Phys. Rev. B* **1986**, *33*, 8822–8824.

57. Becke, A. D. Density-Functional Exchange-Energy Approximation with Correct Asymptotic Behavior. *Phys. Rev. A* **1988**, *38*, 3098–3100.
58. Grimme, S.; Antony, J.; Ehrlich, S.; Krieg, H. A Consistent and Accurate Ab Initio Parametrization of Density Functional Dispersion Correction (DFT-D) for the 94 Elements H-Pu. *J. Chem. Phys.* **2010**, *132*, 154104.
59. Neese, F. The ORCA Program System. *WIREs Comput. Mol. Sci.* **2012**, *2*, 73–78.
60. Becke, A. D. Density-Functional Thermochemistry. III. the Role of Exact Exchange. *J. Chem. Phys.* **1993**, *98*, 5648–5652.
61. Lee, C.; Yang, W.; Parr, R. G. Development of the Colle-Salvetti Correlation-Energy Formula into a Functional of the Electron Density. *Phys. Rev. B* **1988**, *37*, 785–789.
62. Pantazis, D. A.; Chen, X.-Y.; Landis, C. R.; Neese, F. All-Electron Scalar Relativistic Basis Sets for Third-Row Transition Metal Atoms. *J. Chem. Theory Comput.* **2008**, *4*, 908–919.
63. Neese, F.; Wennmohs, F.; Hansen, A.; Becker, U. Efficient, Approximate and Parallel Hartree–Fock and Hybrid DFT Calculations. a "Chain-of-Spheres" Algorithm for the Hartree–Fock Exchange. *Chem. Phys.* **2009**, *356*, 98–109.
64. van Lenthe, E.; Baerends, E. J.; Snijders, J. G. Relativistic Regular Two-Component Hamiltonians. *J. Chem. Phys.* **1993**, *99*, 4597–4610.

65. van Wüllen, C. Molecular Density Functional Calculations in the Regular Relativistic Approximation: Method, Application to Coinage Metal Diatomics, Hydrides, Fluorides and Chlorides, and Comparison with First-Order Relativistic Calculations. *J. Chem. Phys.* **1998**, *109*, 392–399.
66. Klamt, A.; Schüürmann, G. COSMO: a New Approach to Dielectric Screening in Solvents with Explicit Expressions for the Screening Energy and Its Gradient. *J. Chem. Soc., Perkin Trans. 2* **1993**, No. 5, 799–805.